

This is the accepted manuscript made available via CHORUS. The article has been published as:

Submonolayer Ag films on Fe(100): A first-principles analysis of energetics controlling adlayer thermodynamics and kinetics

Wei Li, Li Huang, James W. Evans, and Yong Han

Phys. Rev. B **93**, 155416 — Published 11 April 2016

DOI: [10.1103/PhysRevB.93.155416](https://doi.org/10.1103/PhysRevB.93.155416)

Submonolayer Ag films on Fe(100): A first-principles analysis of energetics controlling adlayer thermodynamics and kinetics

Wei Li¹, Li Huang^{1,*}, James W. Evans^{2,3}, and Yong Han^{2,3†}

¹Department of Physics, South University of Science and Technology of China, Shenzhen, Guangdong 518055, P. R. China

²Department of Physics and Astronomy, Iowa State University, Ames, Iowa 50011, USA

³Ames Laboratory—U. S. Department of Energy, Iowa State University, Ames, Iowa 50011, USA

*huangl@sustc.edu.cn

†yong@ameslab.gov

Epitaxial growth of Ag on Fe(100) and post-deposition relaxation have been studied in several experiments. We provide a [first-principles density functional theory analysis](#) of key adatom interaction energies and diffusion barriers controlling growth and relaxation kinetics for the submonolayer regime, as these have not been assessed previously. A cluster expansion approach is used to [obtain](#) an extensive set of conventional lateral interactions between adatoms on four-fold hollow adsorption sites. We find robust oscillatory decay of pair interactions with increasing separation, and of trio interactions with increasing perimeter length. [First and second nearest-neighbor](#) pair interactions, as well as compact linear and bent trio interactions, dominate. The adatom terrace diffusion barrier is estimated to be $E_d \approx 0.39$ eV. [We also provide a limited analysis of unconventional interactions for which one adatom is at the bridge-site transition state for hopping and one or more others are at four-fold hollow sites. Energy barriers for diffusion along island edges can be determined with the aid of both conventional and unconventional interactions.](#)

PACS Number(s): 68.35.Md, 68.43.Jk, 68.55.A-, 68.35.bd

I. INTRODUCTION

Epitaxial thin films of Ag on Fe(100) are of particular interest for several reasons. *First*, there is a near perfect lattice registry for fcc Ag(100) on bcc Fe(100) with a mismatch of less than 1%. This feature ensures the growth of epitaxial films with an unambiguous well-defined interface, i.e., the first adlayer of Ag is located at four-fold hollow (4fh) sites on Fe(100). Knowledge of the interface structure together with the perfect defect-free fcc (100) epitaxial structure of the Ag thin films on Fe(100) has allowed predictive [first-principles](#) density functional theory (DFT) analyses of the energetics for the supported film by Chou and coworkers [1,2]. This includes precise [determination](#) of the variation of surface energy with increasing film thickness. *Second*, photoemission spectroscopy studies performed by Chiang and coworkers demonstrated electron confinement in the Ag film and associated quantum well states (QWS) [3–5] with unusually weak electron-phonon coupling [6]. Recently, scanning tunneling microscopy (STM) has also been used to probe the QWS as a function of film thickness [7]. *Third*, the presence of QWS introduces a strong thickness-dependence of the stability of flat Ag films [8]. This behavior is consistent with the surface energy analysis of Chou *et al.* [1,2] [Low-energy](#) electron microscopy studies by

Altman and coworkers [9,10] have characterized morphological evolution of a film initially formed out of equilibrium with an unstable thickness towards a mixture of preferred heights.

Despite the substantial interest in the Ag/Fe(100) system, the energetics controlling submonolayer and multilayer thin film growth or post-deposition evolution in this system [have](#) not been systematically analyzed. Here, we will focus on the submonolayer regime and explore energetics associated with island nucleation and growth during deposition, as well as with post-deposition coarsening phenomena. In the traditional picture, the density of islands formed during deposition is controlled by the adatom terrace diffusion barrier, E_d , at lower temperatures (T) corresponding to irreversible island formation, and [also](#) by the interaction between nearest-neighbor (NN) Ag adatom pairs which determines the onset of reversibility at higher T [11]. However, we will find that both long-range pair interactions, which can impact island formation, and many-body interactions are significant for Ag/Fe(100). The long-range interactions oscillate between attractive and repulsive values, a feature which is usually only prominent usually for certain metal (111) surfaces [12,13]. Growth shapes of individual islands and of coalescing pairs of islands during deposition are controlled by the barriers for diffusion along island edges [11]. Post-deposition coarsening of adlayers with separated islands at lower coverages is likely dominated by Smoluchowski ripening, i.e., island diffusion and coalescence both of which are also controlled by edge diffusion [14,15]. Coarsening of incomplete adlayers with isolated pits at high submonolayer coverages may be controlled by vacancy-mediated Ostwald ripening, and thus [dependent on](#) the diffusion barrier and formation energy for isolated advacancies [15].

From the above, it is clear that a comprehensive analysis of adlayer formation and coarsening requires knowledge of both surface thermodynamics (lateral interaction energies and formation energies for adspecies), as well as numerous activation barriers for diffusive hopping of adatoms (including adatom terrace and edge diffusion). Adlayer thermodynamics is determined from conventional lateral adspecies interactions (ω 's) where Ag adatoms are located at 4fh adsorption sites. Previous studies for metal (100) surfaces revealed the possible need to include many-body trio and even [quarto](#) interactions, as well as pair interactions, to accurately describe energetics [16–19]. [As described in more detail in Sec. IV](#), activation barriers for diffusion can be determined with the aid of a distinct set of “unconventional” interactions (ϕ 's) involving one Ag adatom at a bridge-site transition state (TS) for diffusive adatom hopping and the other adatoms are at 4fh sites [18–21]. Validation of this assignment of the TS will [also](#) be provided in Sec IV. Given these activation barriers, corresponding adatom hop rates which provide the basic input to kinetic modeling are determined assuming an Arrhenius form with a standard choice of prefactor $\nu \approx 5 \times 10^{12}/\text{s}$.

Adatom interactions can be systematically determined from analysis of the energetics for large lateral unit cell configurations with an isolated pairs, trios, etc. of adatoms [13]. First, pair interactions are determined from configurations with an isolated adatom pair given knowledge of the isolated adatom adsorption energies and of the substrate energy. Then, trio interactions are determined [by](#) subtracting pair contributions from the total trio interaction energy, etc. Alternatively, cluster-expansion (CE) techniques can be applied

assessing the energies of various adlayer configurations usually with smaller unit cells [17,22,23]. We will mainly utilize the CE approach in this study focusing on a comprehensive determination of conventional ω -interactions. This approach has been successfully applied for systems with long-range ω -interactions [12,24,25], but there are significant challenges which we will discuss. Analysis of ϕ -interactions is rare and involves additional challenges, as will be described, so a more limited analysis is provided.

In Sec. II, we provide the details of our DFT calculations. The comprehensive analysis of conventional ω -interactions is [presented](#) in Sec. III. A more limited analysis of unconventional ϕ -interactions and other related interactions is provided in Sec. IV. Further discussion and application of these results is presented in Sec. V, and conclusions are [offered](#) in Sec. VI.

II. BACKGROUND: SYSTEM PROPERTIES AND DFT ANALYSIS

All DFT total energy calculations reported in this paper were performed using the plane-wave VASP code [26–29]. The projector-augmented-wave (PAW) method [30,31] is used for the electron-core interactions, and the Perdew-Burke-Ernzerhof (PBE) generalized gradient approximation (GGA) functional [32] is used for exchange and correlation, as is typically the case in analysis of metal-on-metal systems yielding considerable success [18–22,24]. The corresponding pseudopotentials were generated and released in 2013 by the VASP group. Due to the strong magnetism of the Fe substrate, spin-polarization effects have been taken into account in all DFT calculations.

As noted in Sec. I, fcc Ag(100) has a near-perfect lattice match with bcc Fe(100) given experimental values for surface lattice constants, a , of $a_{\text{Fe}} = 0.2866$ nm [33] and $a_{\text{Ag}} = 0.2877$ nm [34]. To support the validity of our analysis of Ag/Fe(100) thin film properties, we naturally check in Appendix A that DFT reliably reproduces basic bulk and surface properties of Fe. Often quantum size effects (QSE) [35] due to finite slab thickness are quite persistent for metal (100) systems [36], so the common selection of 5–6 atomic layers (referred to below as monolayer or ML) [for](#) slabs is not sufficient [37,38]. Given this concern, we perform benchmark analyses of the slab thickness dependence for key quantities such as surface energy and magnetic moment to assess how quickly they converge to bulk values with increasing Fe(100) slab thickness. In fact, this convergence is rather slow (see again Appendix A) prompting the use of a 15-ML slab in our main analyses of surface energetics. Thus, the calculations are demanding, the maximal number of [Fe](#) atoms involved in our analysis for a 4×4 lateral unit cell being 240, plus any [Ag](#) adatom(s). Additional tests of the thickness-dependence of energies of interest are described in Appendix B.

Our DFT analysis focuses on the energetics for various Ag adlayer configurations with $n \times m$ lateral unit cells on thick slabs representing Fe(100) substrates. The key quantity extracted is the adlayer energy per Ag atom, $E_{n \times m}^{\beta}$, corresponding to the configuration β which has M Ag atoms per unit cell with the adlayer coverage $M/(nm)$. This adlayer energy equals the sum of the total adsorption plus the total lateral interaction energy within the cell divided by M . It is obtained from

$$E_{n \times m}^{\beta} = (E_{\text{tot}} - E_{\text{slab}} - ME_{\text{Ag}})/M, \quad (1)$$

where E_{tot} is the total energy of Fe slab plus Ag adlayer atoms, E_{slab} is the energy of the Fe slab without Ag adlayer atoms, and E_{Ag} is the self-energy of an isolated gas-phase Ag atom. E_{tot} , E_{slab} , and E_{Ag} are directly obtained from DFT calculations.

In the following Sections, the superscript β in $E_{n \times m}^{\beta}$ has the form $ihjb$, indicating that i Ag atoms are at 4fh sites and j Ag atoms are at bridge sites within each unit cell where $i + j = M$, but jb (or ih) is omitted when $j = 0$ (or $i = 0$). Also, sometimes the subscript $n \times m$ will be augmented to provide additional information on adlayer structure. By way of example, $E_{n \times n}^{1h}$ indicates a $p(n \times n)$ structure with $M = 1$ Ag adatom at a 4fh site, $E_{n \times n}^{1b}$ indicates a $p(n \times n)$ structure with $M = 1$ Ag adatom at a bridge site, $E_{c(2 \times 2)}^{2h}$ indicates a $c(2 \times 2)$ adlayer with $M = 2$ Ag atoms at two 4fh sites, $E_{4 \times 4, \text{label}}^{1h1b}$ indicates a 4×4 adlayer with $M = 2$ Ag atoms: one at a 4fh site and one at a bridge site (where “label” will identify the specific adlayer motif, see below), etc.

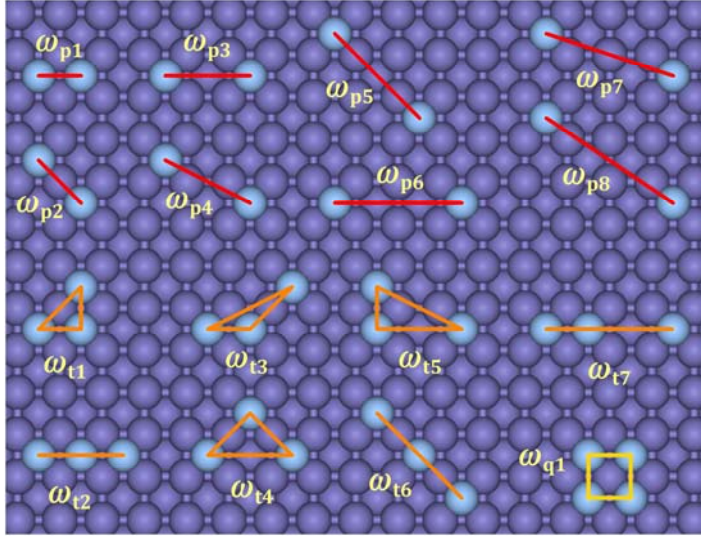
When evaluating ω -interactions using 15-ML Fe(100) slab as the substrate, the bottommost 10 ML of the slab are fixed corresponding to bulk bcc structure with the optimized lattice constant $a = 0.2830$ nm. The topmost 5-ML Fe(100), as well as any Ag atoms at 4fh sites, are fully relaxed. For evaluation of ϕ -interactions, the only difference is that the x or y coordinate of the Ag atom on the bridge site is fixed to avoid its possible movement to a neighboring 4fh site during relaxation of the other degrees of freedom. Negative (positive) values of ω and ϕ correspond to attractive (repulsive) interactions. In these calculations, the energy cutoffs for the plane wave basis are set to be default value 267.882 eV for an Ag-Fe system, and vacuum thickness between two adjacent periodic slabs along the z direction is taken to be 1.5 nm. For accuracy in energy minimization, we take 0.1 eV/nm as the force-convergence criterion. The choice of \mathbf{k} mesh (see Appendix B) depends on supercell size with careful tests for reaching energy convergence. Spurious dipole-dipole interactions between slab replicas due to periodic boundary conditions are also checked to be negligibly small and therefore not taken into account in our analysis of the Ag-Fe system.

Our analysis will assume that Ag remains on the Fe(100) surface as one or more adatoms rather than exchanging with the substrate. To support this assumption, we assess the thermodynamics of Ag-Fe exchange on the Fe(100) surface. Using a 4×4 unit cell with a 15-ML Fe(100) slab, we obtain an energy increase of $\Delta E = 0.564$ eV upon exchanging an Ag adatom at a 4fh site with a surface Fe atom (so that the Fe atom becomes an adatom at a 4fh site). We also used a 5-ML slab with bottommost 1-ML Fe atoms fixed and obtain $\Delta E = 0.608$ eV. These results indicate that such Ag-Fe exchange is strongly disfavored thermodynamically. Thus, such exchange is not considered further in this work.

III. CONVENTIONAL ω -INTERACTIONS: ADLAYER THERMODYNAMICS

For ω -interactions between adatoms at 4fh sites, we will use the notation ω_{pi} for pair interactions where separation, $d = d_{12}$, increases with i . Specifically, one has $d_{12} = a, \sqrt{2}a, 2a, \sqrt{5}a, 2\sqrt{2}a, 3a, \sqrt{10}a, \sqrt{13}a, \dots$ for $i = 1, 2, 3, \dots$ respectively. Trio interactions are denoted by ω_{ti} where the total perimeter length $d = d_{123}$ for the trio-motif increases with i .

For linear trio configurations, d_{123} is taken as twice their length. Thus, one has $d_{123} = (2 + \sqrt{2})a \approx 3.414a$, $4a$, $(1 + \sqrt{2} + \sqrt{5})a \approx 4.650a$, ... for $i = 1, 2, 3, \dots$, respectively. Quarto interactions are denoted by ω_{qi} where the perimeter length $d = d_{1234}$ increases with i , and $d_{1234} = 4a$ for $i = 1$ corresponding to a square motif. See Fig. 1. Undoubtedly, the NN pair interaction, ω_{p1} , will dominate other interactions. We suggest that the magnitudes of the second NN pair interaction, ω_{p2} , the bent trio, ω_{t1} , and linear trio, ω_{t2} , while well below $|\omega_{p1}|$, will be significantly above those of other interactions. Our detailed analysis will confirm this picture. Our claim regarding the relative magnitude of interactions implies that the magnitude of the linear trio $|\omega_{t2}|$ exceeds that for the third NN pair $|\omega_{p3}|$, even though both motifs have the same linear span of $2a$. We note that this perhaps unintuitive



feature was seen in previous DFT analysis for Cu/Cu(100) [16].

FIG. 1. (Color online) Conventional pair interactions ω_{pi} , trio interactions ω_{ti} , and quarto interaction ω_{q1} , labeled so that the separation d_{12} or perimeter length d_{123} increase with increasing $i = 1, 2, 3, \dots$

As indicated in Sec. I, we will primarily rely on the CE approach [17,22,23] to determine the ω 's. Suppose that adlayer energies are to be described using N ω 's together with the adsorption energy, E_{4fh} , of an isolated Ag adatom at a 4fh site. The basic procedure selects $N + 1$ suitable adlayer configurations for which the energy per adatom is obtained directly from DFT calculations. Then, expressing the $N + 1$ energies in terms of the ω 's and E_{4fh} allows determination of these parameters by solving $N + 1$ linear equations for $N + 1$ unknowns. Detailed implementation of this approach might be tailored to the specific application. For example, one could first determine E_{4fh} independently and directly from a large-unit cell $p(n \times n)$ configuration with negligible interactions between adatoms, and consequently determine the ω 's from the energies of N other configurations. Then, these effective ω 's exactly recover the energies of the selected adlayer configurations, but incorporate the effect of neglected longer-range pair or many-body interactions. Alternatively, using smaller unit cells for all $N + 1$ selected configurations would in general yield an effective value of E_{4fh} incorporating neglected longer-range interactions. As a result, the effect of these neglected interactions might at least partly cancel in the

evaluation of ω 's, producing estimates that more accurately reflect the true ω 's. Appendix C gives a simple example of this cancellation effect. We mainly utilize this alternative strategy in our study.

For reference, we provide the energies per Ag atom, $E_{n \times n}^{1h}$, for $p(n \times n)$ configurations with one Ag atom per unit cell at a 4fh site and Ag adlayer coverage of $1/n^2$ ML on the 15-ML Fe(100) slab: $E_{1 \times 1}^{1h} = -2.853$, $E_{2 \times 2}^{2h} = -2.483$, $E_{3 \times 3}^{1h} = -2.496$, and $E_{4 \times 4}^{1h} = -2.529$ (in eV). With increasing n , the value of $E_{n \times n}^{1h}$ approaches the true adsorption energy, E_{4fh} , of an isolated Ag adatom at a 4fh site. Some analysis of the dependence of these energies on Fe(100) slab thickness is provided in Appendix B.

It is appropriate to note that various validation procedures are often applied for CE analyses. We will utilize the so-called leave- n_v -out cross-validation method [17,39] where one chooses various subsets of $N + 1$ configurations out of a total of $N + 1 + n_v$ configurations to determine the N ω 's and E_{4fh} . Comparing results for different choices of the n_v omitted configurations clarifies reliability of the results. We also note that there are various automated procedures attempting optimal selection of both the configurations and the ω 's [23], but these will not be utilized here.

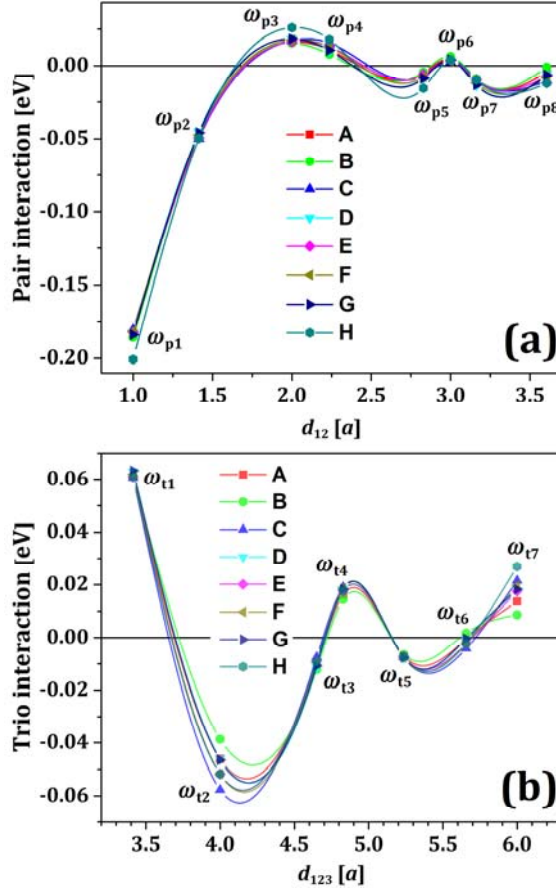
A. Preliminary simplified modeling with four ω 's

As noted above, we expect that ω_{p1} , ω_{p2} , ω_{t1} , and ω_{t2} will be the dominant interactions for metal (100) surfaces. Thus, a simplified analysis might use a $p(n \times n)$ configuration for some $n \geq 2$ to determine E_{4fh} , and then four other configurations to determine the four ω 's. Selecting configurations: (i) $p(1 \times 1)$ with coverage 1 ML and adlayer energy $E_{1 \times 1}^{1h} = -2.853$ eV **per Ag atom**, (ii) $c(2 \times 2)$ with coverage 1/2 ML and $E_{c(2 \times 2)}^{1h} = -2.556$ eV, (iii) $p(2 \times 1)$ with coverage 1/2 ML corresponding to single-atom wide rows, $E_{2 \times 1}^{1h} = -2.696$ eV, and (iv) 3×1 with coverage 2/3 ML corresponding to double-atom wide rows and $E_{3 \times 1}^{2h} = -2.754$ eV, this approach yields $\omega_{p1} = -0.173$ (-0.127), $\omega_{p2} = -0.036$ (-0.014), $\omega_{t1} = +0.032$ ($+0.009$), and $\omega_{t2} = -0.040$ (-0.040) in eV using $n = 2$ ($n = 4$) for E_{4fh} . See Appendix C for further details. These values appear reasonable although there is a strong dependence on the selected E_{4fh} . This dependence presumably results from the neglect of multiple longer-range pair interactions and also other trio interactions. This prompts the implementation of a refined analysis retaining a more extensive set of ω -interactions as presented below in Sec. III B.

B. Refined CE analysis with sixteen ω 's

Our more extensive CE modeling of the Ag/Fe(100) system incorporates a larger set of sixteen interactions including 8 pairs, 7 trios, and 1 quarto shown in Fig. 1. We use subsets of 17 configurations selected out of a larger set of 20 configurations with unit cells sizes including 1×1 , 2×1 , 3×1 , 2×2 , 3×2 , 4×2 , 3×3 , ... to determine the sixteen ω 's and E_{4fh} . See Appendix B for the 20 configurations. We emphasize that E_{4fh} is determined from these smaller unit cell configurations versus a large unit-cell $p(n \times n)$ configuration with $n \geq 4$, and will thus correspond to an effective value. Results from 8 different choices of 17 configurations out of 20 are shown in Fig. 2(a) for pair interactions and in Fig. 2(b) for trio

interactions. Often for this type of leave-3-out cross-validation analysis, one assesses the error in energy for neglected configurations for each choice of retained configurations, and then just reports averaged results for various choices with lower errors. However, since our results vary little with the choice of left-out configurations, we report pair and trio interactions for all 8 choices of retained configurations. The value of the quarto interaction ω_{q1} varies between -0.02 and -0.05 eV with an average value of -0.039 eV. Average values of ω -interactions from these 8 choices are presented in Table I. As suggested [above](#),



ω_{p1} , ω_{p2} , ω_{t1} , and ω_{t2} are in fact the dominant interactions.

FIG. 2. (Color online) (a) Conventional pair interactions versus separation $d = d_{12}$. (b) Conventional trio interactions versus $d = d_{123}$. The configurations used for the leave-3-out analyses A–H are indicated in Appendix B.

From Fig. 2(a), the robust oscillatory decay of the lateral pair interactions for larger separations in this Ag/Fe(100) system is immediately apparent, specifically these interactions [oscillating](#) between attractive and repulsive values. The presence of these significant longer-range pair interactions, as well as several significant values of trio interactions, makes it clear the limitations of the simplified analysis of Sec. III A. In Fig. 2(b), we naturally plot trio interactions as a function of the perimeter $d = d_{123}$ of the [trio motif](#). This choice is motivated by theoretical analysis of the expected variation of interactions

with motif size [17,40], and shown to be effective in other DFT analyses of metal-adatom interactions for various surfaces [24,41]. Again one finds systematic oscillatory behavior, although the ω_{t7} values in Fig. 2(b) for the largest perimeter length $d_{123} = 6a \approx 1.73$ nm are not expected to be reliable.

TABLE I. Average values of conventional ω -interactions for the leave-3-out analyses of A–H described in Appendix B. Values is rounded to 3 significant figures after the decimal point. As noted in the text, the value of ω_{t7} is likely inaccurate.

ω_{p1}	ω_{p2}	ω_{p3}	ω_{p4}	ω_{p5}	ω_{p6}	ω_{p7}	ω_{p8}
-0.185	-0.048	+0.018	+0.012	-0.008	+0.004	-0.011	-0.007
ω_{t1}	ω_{t2}	ω_{t3}	ω_{t4}	ω_{t5}	ω_{t6}	ω_{t7}	ω_{q1}
+0.062	-0.049	-0.010	+0.018	-0.007	-0.001	+0.018	-0.040

We recall that this type of prominent longer-range oscillatory behavior is often seen for adsorbates on various metal (111) surfaces [12,13]. In general, electronic indirect (through surface) interactions can have oscillatory Friedel behavior controlled by the Fermi wave vector. Usually the strength of the pair interactions decays quickly like d^{-5} , so that oscillations are not apparent. However, in the presence of a metallic surface state, i.e., a surface band that crosses the Fermi level, as is common on the (111) faces of noble metals, the decay can be much slower like d^{-2} for pair interactions and like $d^{-2/3}$ for trio interactions [17,40]. Long-range oscillatory interactions are typically not prominent on metal (100) surfaces.

C. Additional analysis and discussion

True versus effective E_{4fh} : The refined analysis in Sec. III B simultaneously determines E_{4fh} together with the ω 's from the energies of mainly small unit-cell configurations. This yields an effective value of $E_{4fh} \approx -2.504$ eV with small variance of ± 0.001 eV. This certainly differs from the true value of E_{4fh} which should be closer to $E_{4 \times 4}^{1h} = -2.529$ eV. Thus, as discussed above and in Appendix C, the effective E_{4fh} must incorporate a contribution from the neglected longer-range pair and trio interactions, a feature which may result in more reliable ω -estimates due to cancellation effects. Indeed, reanalysis of the sixteen ω 's by setting $E_{4fh} = E_{4 \times 4}^{1h}$ and selecting sixteen configurations from the 20 used in Sec. III B yields rather different and less satisfactory results than those shown in Fig. 2. For example, pair interactions do not decay smoothly for large $d = d_{12}$, but retain significant positive (repulsive) values partly compensating for the more negative value of E_{4fh} .

More direct analysis of ω 's: Despite the consistency of results for ω -interactions from the procedure of Sec. III B, it is instructive to alternatively consider more direct analysis to further support these results. Such more direct analysis can be based on the use of

appropriate selected larger unit-cell configurations. Here, we just present two examples. First, a more direct estimate of ω_{p3} follows from the relation

$$\omega_{p3} + \omega_{p5} \approx (E_{2 \times 2}^{1h} - E_{4 \times 4}^{1h})/2 = +0.023 \text{ eV} \quad (2)$$

yielding $\omega_{p3} \approx 0.02 \text{ eV}$ if one sets $\omega_{p5} \approx 0$. This estimate is reasonably consistent with the mean estimate $\omega_{p3} \approx +0.018 \text{ eV}$ in Table I. Second, a more direct estimate of ω_{p2} can be obtained from analysis of the energy per adatom, $E_{n \times n, p2}^{2h}$, of a configuration containing a single isolated second NN adatom dimer in a large $n \times n$ unit cell. Using $E_{4 \times 4, p2}^{2h} = -2.539 \text{ eV}$, one has that

$$\omega_{p2} + 2\omega_{p7} \approx 2(E_{4 \times 4, p2}^{2h} - E_{4 \times 4}^{1h}) = -0.020 \text{ eV}. \quad (3)$$

Using $E_{4 \times 4}^{1h} \approx E_{4 \times 4}^{1h} = -2.529 \text{ eV}$ yields an estimate of $\omega_{p2} \approx -0.020 \text{ eV}$ assuming that $\omega_{p7} \approx 0$ (cf. the mean estimate of $\omega_{p2} \approx -0.048 \text{ eV}$ in Table I from Sec. III B).

Comparison with other metal (100) systems: It is instructive to compare the behavior of the dominant ω -interactions for Ag/Fe(100) with that in other metal (100) systems. Previous analysis for Cu/Cu(100) [16] reveals that $\omega_{p1} = -0.332$, $\omega_{p2} = -0.043$, $\omega_{t1} = +0.054$, and $\omega_{t2} = -0.016$ (in eV) are the dominant interactions, although $\omega_{p3} = -0.013 \text{ eV}$ is just slightly smaller than ω_{t2} for this system. For Ag/Ag(100), one finds that $\omega_{p1} = -0.283$, $\omega_{p2} = -0.027$, $\omega_{t1} = +0.032$, and $\omega_{t2} = -0.016$ (in eV) [18], the slightly lower magnitudes reflecting the smaller bulk cohesive energy for Ag than for Cu. Thus, the trends in these interactions are similar to those for Ag/Fe(100) for which ω_{p1} is relatively weaker. However, for Au/Ag(100), ω_{p2} becomes repulsive, and the magnitude of the attractive trio ω_{t2} is enhanced relative to other interactions [18,19].

Decomposition of ω 's into electronic and elastic components: In the above analyses of configuration energies, both the topmost 5-ML Fe atoms of the substrate and the adlayer Ag atoms are relaxed. The ω -interactions obtained therefrom are the total (electronic + elastic) values. An effective procedure to directly determine just the electronic component is simply to perform the analysis with substrate Fe atoms frozen at their relaxed positions in the absence of Ag adlayer, but Ag atoms of the adlayer still relaxed [12,13,24,41,42]. The elastic component then is given by the difference between the total interaction and the electronic component. We have performed such a comparative analysis by selecting two short-range pairs and one bent trio configuration using a larger unit cell of 5×5 which makes computation more expensive. Nonetheless, we still perform analysis for 4-, 8-, and 12-ML Fe(100) slabs to reliably assess limiting behavior for a semi-infinite slab. For details, see Appendix D. The elastic component remains significant, so the behavior for Ag on Fe(100) surface appears to be intermediate between that for a fcc (111) surface where electronic interactions dominate [12,13,24] and that for a fcc (110) surface where elastic interactions may dominate [41,42]. From this behavior, the strength of the elastic effect also indicates how close the packings of the 3 types of surface lattice are: (111) surface is most close-packed with hexagon lattice, (110) surface is least close-packed with rectangular lattice, while (100) surface is intermediately close-packed with square lattice. In addition, it is appropriate to note that results from the above CE analysis are closer to the values for electronic component from a large-unit-cell calculation than the total

interaction. This presumably reflects the feature that the CE analysis makes extensive use of small-unit-cell configurations where relaxation of substrate atoms is actually constrained.

IV. UNCONVENTIONAL ϕ -INTERACTIONS AND SURFACE DIFFUSION KINETICS

First, we present the result of our analysis of the terrace diffusion barrier, E_d , for isolated Ag adatoms on Fe(100), and also discuss more general surface diffusion processes for non-isolated adatoms. We first estimate the TS energy, E_{br} , for an Ag adatom adsorbed at the bridge site for hopping. Using a $p(4 \times 4)$ unit cell and 15-ML Fe(100) slab, we obtain

$$E_{br} \approx E_{4 \times 4}^{1b} = -2.141 \text{ eV.} \quad (4)$$

Then E_d is simply estimated from

$$E_d = E_{br} - E_{4fh} \approx E_{4 \times 4}^{1b} - E_{4 \times 4}^{1h} = 0.388 \text{ eV,} \quad (5)$$

where

$$E_{4fh} \approx E_{4 \times 4}^{1h} = -2.529 \text{ eV.} \quad (6)$$

As noted in Sec. II, the exchange between an Ag adatom and surface Fe atoms is strongly disfavored thermodynamically, so exchange diffusion is not a competitive pathway.

Next, consider hopping of Ag adatoms in general local environments, e.g., along the edge of an island, where the pathway is always between neighboring stable 4fh sites through a bridge-site transition state. For an isolated adatom, symmetry suggests that the TS is exactly at the bridge site, and this is confirmed by more detailed analysis, e.g., using a climbing nudged elastic band (cNEB) method [43]. In general, the TS will be slightly shifted from the ideal bridge-site position due to the influence of other nearby adatoms. However, the strong modulation of the adatom binding energy on (100) surfaces, suggests that this shift will be small, contrasting hexagonal close-packed surfaces. We have confirmed this proposal by performing selected cNEB analyses of minimum-energy diffusion paths for various diffusion processes and local environments, e.g., diffusion along close-packed step edges, detachment from such step edges, corner rounding, dimer diffusion, vacancy diffusion in an island, etc. We find that the TS for all these diffusion processes is always at or very close to the bridge site. As an example, we obtain an adatom shift of only ~ 0.02 nm towards the edge for the diffusion along a straight step edge of double chain using a 4×2 unit cell and 4-ML Fe(100) slab, while the adatom shift is ~ 0.008 nm away from the edge for the detachment perpendicular to a double chain step using a 5×2 unit cell.

Finally, we describe an approach to precisely determine activation barriers, E_{act} , for general local environments [18–21]. If Φ_{init} denotes total lateral interaction energy in the initial state with the adatom at a 4fh site before hopping, and Φ_{TS} denotes the total interaction energy in the TS, then it follows that

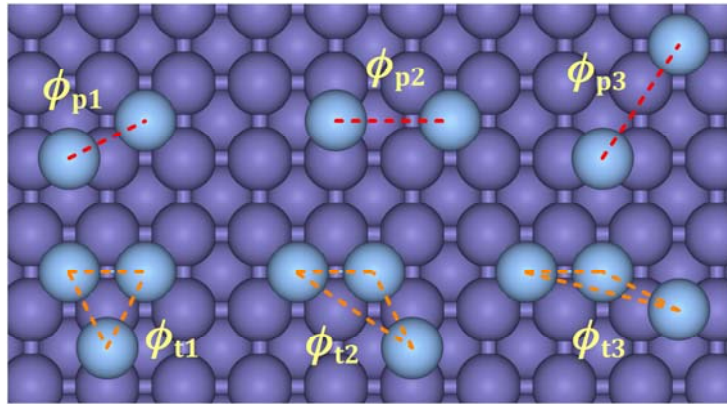
$$E_{act} = E_d + \Phi_{TS} - \Phi_{init}. \quad (7)$$

Summing over relevant conventional ω 's immediately determines the total interaction energy Φ_{init} . In Sec. I, we have already mentioned unconventional ϕ -interactions which involve one Ag adatom at a bridge site which is taken as the TS for diffusive hopping and

one or more other adatoms at 4fh sites. By analogy with determination of Φ_{init} , summing over relevant ϕ 's determines the total interaction energy, Φ_{TS} , at the TS. Thus, knowledge of all of E_d , ω 's, and ϕ 's allows precise determination of general E_{act} . Given the barrier E_{act} , the corresponding rate for hopping is taken to have the Arrhenius form $h = \nu e^{-E_{\text{act}}/(k_B T)}$ where k_B is Boltzmann's constant, T is the surface temperature, and a common prefactor or attempt frequency is often selected as $\nu \approx 5 \times 10^{12}/\text{s}$ for all hops [18–21].

It has in fact long been recognized that E_{act} is determined by distinct interactions at the TS [44]. For metal (100) systems, a study based on semi-empirical potentials offered a reasonable hypothesis for the dominant unconventional pair interaction [45]. Another study was the first to use DFT to directly assess such interactions for Al diffusion on Al(110) in the presence of a single nearby adatom [46]. By extending these ideas further, a systematic formalism to determine general E_{act} has been provided and implemented [18–21]. We should contrast this approach with the much more common approximate determinations of E_{act} based on E_d and just knowledge of ω 's. The simplest “initial-value approximation” just sets $E_{\text{act}} = E_d - \Phi_{\text{init}}$, but symmetric versions of Bronsted-Evans-Polyani or Butler-Volmer approximations in addition utilize the total lateral interaction Φ_{final} at the final state after hopping which is also determined from summing ω 's [12]. However, these approximate choices fail dramatically to describe edge diffusion processes in metal (100) systems [11,18]. They predict the diffusion barrier along close-packed edges to be equal to or higher than E_d , whereas it is generally much lower.

For unconventional pair interactions, we will use the notation ϕ_{pi} where separation, $d = d_{12}$, increases with i , so that $d_{12} = \sqrt{5}a/2 \approx 1.118a$, $3a/2$, $\sqrt{13}a/2 \approx 1.803a$, ... for $i = 1, 2, 3, \dots$ respectively. Trio interactions are denoted by ϕ_{ti} where the total perimeter length $d = d_{123}$ for the trio-motif increases with i , so that $d_{123} = (1 + \sqrt{5})a \approx 3.236a$, $(1 + \sqrt{5}/2 + \sqrt{13}/2)a \approx 3.921a$, $(1 + \sqrt{5}/2 + \sqrt{17}/2)a \approx 4.180a$, ... for $i = 1, 2, 3, \dots$, respectively. See Fig. 3 for these motifs. Note that ϕ_{p1} and ϕ_{t1} are the strongest interactions, and these will largely control the barrier for diffusion along close-packed

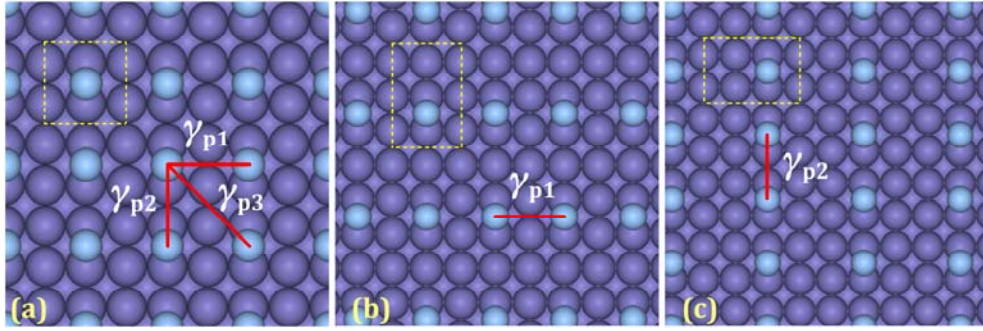


edges.

FIG. 3. (Color online) Examples of unconventional pair interactions, ϕ_{pi} , and trio interactions, ϕ_{ti} , with one adatom at a bridge site and the others at 4fh sites.

A. CE analysis for ϕ 's and related issues

First, we comment on a CE approach to determine the ϕ 's. This approach involves calculating the energies of various adlayer configurations with $n \times m$ unit cells, each of which includes one atom at a bridge site and any others at 4fh sites. While this approach has not been implemented previously [for *unconventional* interactions](#), the basic strategy just mimics that for conventional interactions. However, one extra complication is that smaller unit cells when periodically extended result in interacting pairs of adatoms at bridge sites. We denote this distinct type of unconventional pair interactions between such bridge pairs by γ_p 's. As a simple example, consider a p(2 \times 2) configuration with Ag on bridge sites as shown in Fig. 4(a). Here, there are two distinct γ_p interactions both for separation $d = 2a$. In one (called γ_{p1}), the two bridge sites are separated by two NN 4fh sites and in the other (called γ_{p2}) by two NN top sites. Study of analogous interactions in O-chemisorption systems indicates that γ_{p1} and γ_{p2} could have significantly different values



[47]. It is possibly also necessary to consider various other unconventional many-body interactions, e.g., with two adatoms at bridge sites with one or two at 4fh sites (i.e., trio γ_t 's or quarto γ_q 's). Strictly speaking, one even needs to consider trio ξ_t 's, quarto ζ_q 's, ... interactions with 3, 4, ... Ag atoms at bridge sites.

FIG. 4. (Color online) (a) Examples of unconventional γ -type interactions involving a pair of adatoms at bridge sites in p(2 \times 2) adlayer structure. (b) p(2 \times 3) adlayer structure. (c) p(3 \times 2) adlayer structure. Dashed frames denote the unit cells.

The above discussion already indicates significant complications in a CE analysis of ϕ -interactions beyond that seen for ω -interactions. However, in attempting to implement such an analysis, there is an additional challenge which might not be anticipated as we now describe. As a preliminary remark, we first note that it is possible to perform a separate self-contained analysis of unconventional interactions with all adatoms on bridge sites. In principle, this analysis is no more complicated than that of ω -interactions. We proceed with such an analysis determining the energies $E_{2 \times 3}^{1b} = -2.054$ eV for p(2 \times 3) and $E_{3 \times 2}^{1b} = -2.065$ eV for a p(3 \times 2) configurations with the Ag adatom on a bridge site. See Figs. 4(b) and 4(c) for these two configurations. Then, neglecting γ_p 's for separation $d \geq 3a$, one obtains that $\gamma_{p1} - \gamma_{p2} = +0.012$ eV, i.e., the difference between these two $d = 2a$ interactions is comparable in magnitude to $\omega_{p3} = +0.018$ eV also with $d = 2a$. Using $E_{4 \times 4}^{1b} = -2.141$ eV and still neglecting γ_p 's for $d \geq 3a$, one then obtains

$$\gamma_{p1} = +0.087 \text{ eV and } \gamma_{p2} = +0.076 \text{ eV,} \quad (8)$$

both far larger than $|\omega_{p3}|$. After also determining the energy $E_{2 \times 2}^{1b} = -2.058$ eV of the $p(2 \times 2)$ configuration in Fig. 4(a), one finds that the longer-range interaction γ_{p3} for $d = 2\sqrt{2}a \approx 2.828a$ is -0.040 eV. Thus, the magnitude of γ_{p3} is far above that of $\omega_{p5} = -0.008$ eV for which also $d = 2\sqrt{2}a$, and is still significantly larger than $|\omega_{p3}|$. The unusual strength of the γ_p 's relative to the ω_p 's might be associated with the feature that the adatoms are less strongly bound to the substrate, and thus more strongly interacting. In any case, these large longer-range γ -interactions naturally lead to significant difficulties in extracting reliable results from a CE approach. Thus, the above neglect of γ_p 's for $d \geq 3a$ may be questionable.

B. Alternative analysis

Given the challenges described above with the CE approach to determine ϕ -interactions, we focus on a more direct analysis based on determination of the energetics of selected larger-unit-cell configurations. Our focus will be on determination of ϕ_{p1} , ϕ_{p2} , and ϕ_{t1} , anticipating that these dominate other ϕ -interactions. In the analysis below, we will always use $E_{4fh} \approx E_{4 \times 4}^{1h} = -2.529$ eV and $E_{br} \approx E_{4 \times 4}^{1b} = -2.141$ eV. It will be important here to use accurate “true” values of these quantities rather than, e.g., the effective value of E_{4fh} obtained in Sec. III.

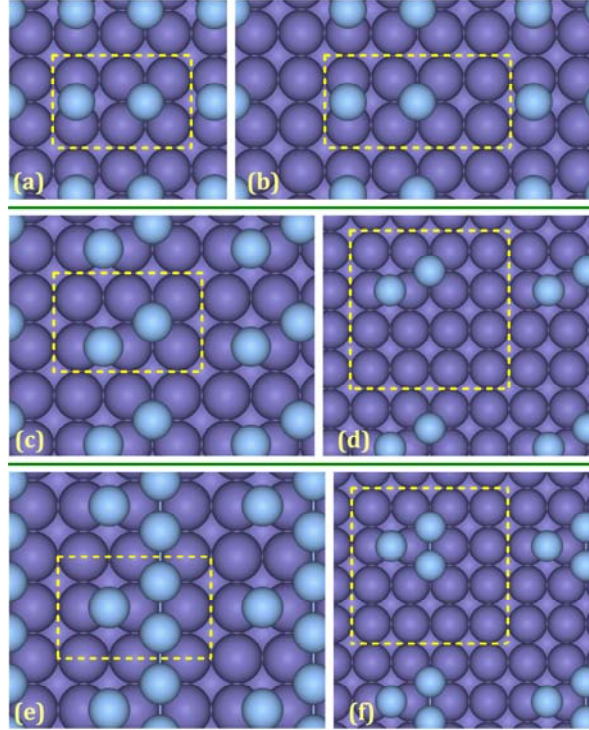


FIG. 5. (Color online) Configurations for: (a) 3×2 and (b) 4×4 cells used to assess ϕ_{p2} ; (c) 3×2 and (d) 4×4 cells used to assess ϕ_{p1} ; (e) 3×2 and (f) 4×4 cells used to determine ϕ_{t1} .

A fairly simple direct analysis is possible for the weak pair interaction ϕ_{p2} for $d = 3a/2$ utilizing the 3×2 and 4×2 configurations including two Ag atoms per unit cell with the energy per Ag atom of $E_{3 \times 2, p2}^{1h1b} = -2.286$ eV and $E_{4 \times 2, p2}^{1h1b} = -2.281$ eV, respectively. See Figs. 5(a) and 5(b) for these two configurations. Neglecting ϕ_p 's for $d \geq 5a/2$, one obtains

$$\phi_{p2} \approx 2(E_{3 \times 2, p2}^{1h1b} - E_{4 \times 2, p2}^{1h1b}) = -0.010 \text{ eV}. \quad (9)$$

Next, we consider the estimation of dominant short-range pair interaction, ϕ_{p1} , based on analysis of the energies, $E_{n \times m, p1}^{1h1b}$, of $n \times m$ unit cells, each of which contains a single isolated ad-dimer of separation $d = \sqrt{5}a/2$ with one adatom at a bridge site and other at a 4fh site. Using a 3×2 unit cell, see Fig. 5(c), for which $E_{3 \times 2, p1}^{1h1b} = -2.367$ eV together with the relation

$$2E_{3 \times 2, p1}^{1h1b} = E_{4fh} + E_{br} + \omega_{p3} + \gamma_{p1} + \phi_{p1} + \dots \quad (10)$$

and values for ω_{p3} , γ_{p1} , E_{4fh} and E_{br} as above, we obtain $\phi_{p1} \approx -0.171$ eV. Here we neglect interactions not indicated explicitly in Eq. (10), the strongest of them being likely ϕ_{p3} for $d = \sqrt{13}a/2$. Using instead an $n \times n$ unit cell for which $E_{n \times n, p1}^{1h1b} = -2.376$ (-2.418) eV for $n = 3$ (4) together with the relation

$$2E_{n \times n, p1}^{1h1b} = E_{4fh} + E_{br} + \phi_{p1} + \dots \quad (11)$$

we obtain $\phi_{p1} = -0.083$ (-0.167) eV for $n = 3$ (4), neglecting interactions not listed explicitly in Eq. (11). The $n = 3$ estimate is likely corrupted by the neglect of significant repulsive γ_p 's for $d = 3a$. However, the estimates for 3×2 and 4×4 cells consistently suggest a reasonable value of $\phi_{p1} \approx -0.17$ eV. The 4×4 cell is illustrated in Fig. 5(d).

Finally, we consider the estimation of the dominant trio interaction, ϕ_{t1} , based on analysis of the energies, $E_{n \times m, t1}^{2h1b}$, of $n \times m$ unit cells containing the corresponding triangular trio motif. For the rather small 3×2 unit cell containing this motif shown in Fig. 5(e), one has that $E_{3 \times 2, t1}^{2h1b} = -2.586$ eV which is given by the relation

$$3E_{3 \times 2, t1}^{2h1b} = 2E_{4fh} + E_{br} + 2\omega_{p1} + 2\omega_{p3} + 2\omega_{t2} + 2\phi_{p1} + \gamma_{p1} + \phi_{t1} + 2\phi_{t2} + \dots \quad (12)$$

This implies that

$$\phi_{t1} \approx -2\phi_{t2} + 0.118 \text{ eV} \quad (13)$$

using E_{4fh} and E_{br} from above, ω_{p1} , ω_{p3} , and ω_{t2} from Table I, $\phi_{p1} = -0.167$ eV from Eq. (11), and γ_{p1} from Eq. (8). From a previous study of Ag and Au on Ag(100) [18], we anticipate that ϕ_{t2} is attractive (with a negative value), so that ϕ_{t1} must be a significant repulsive interaction (with a positive value). For isolated triangular motifs in a 4×4 unit cell shown in Fig. 5(f), the energy $E_{4 \times 4, t1}^{2h1b} = -2.531$ eV is given with the relation

$$3E_{4 \times 4, t1}^{2h1b} = 2E_{4fh} + E_{br} + \omega_{p1} + 2\phi_{p1} + \phi_{t1} + \dots \quad (14)$$

Using E_{4fh} and E_{br} from above, as well as ω_{p1} in Table I and $\phi_{p1} = -0.167$ eV from Eq. (11), Eq. (14) indeed implies strong repulsive $\phi_{t1} \approx +0.125$ eV, which together with Eq. (13) implies that $\phi_{t2} \approx -0.004$ eV.

V. APPLICATIONS OF RESULTS FOR ENERGETICS

We present four diverse applications of the above analyses of energetics:

(i) *Adlayer thermodynamics.* The formation energy for an adatom, $E_{\text{form}}(\text{ad}) = E_{4\text{fh}} - E_{1\times 1}^{1\text{h}} \approx E_{4\times 4}^{1\text{h}} - E_{1\times 1}^{1\text{h}}$, corresponds to the lateral interaction energy per atom in a large island [37,48]. To provide another perspective, $E_{\text{form}}(\text{ad})$ also corresponds to the energy cost to move an adatom from an isolated kink site on an otherwise straight close-packed step edge to the terrace. Either formulation implies that

$$E_{\text{form}}(\text{ad}) = -2\omega_{\text{p}1} - 2\omega_{\text{p}2} - 2\omega_{\text{p}3} - 4\omega_{\text{p}4} - 2\omega_{\text{p}5} - 2\omega_{\text{p}6} - 4\omega_{\text{p}7} - 4\omega_{\text{p}8} - \dots \\ -4\omega_{\text{t}1} - 2\omega_{\text{t}2} - 8\omega_{\text{t}3} - 4\omega_{\text{t}4} - 8\omega_{\text{t}5} - 2\omega_{\text{t}6} - 4\omega_{\text{t}7} - \dots - \omega_{\text{q}1} - \dots \approx 0.349 \text{ eV}. \quad (15)$$

As an aside, it is sometimes instructive to define an effective NN interaction so that the lateral interaction energy per atom in a large island corresponds to $2\omega_{\text{p}1}^{\text{eff}}$. Thus, it follows that $\omega_{\text{p}1}^{\text{eff}} = -E_{\text{form}}(\text{ad})/2 \approx -0.175 \text{ eV}$.

The formation energy for an isolated vacancy, $E_{\text{form}}(\text{vac})$, corresponds to the energy cost to move an atom from the center of a large island to a kink site on an otherwise close-packed step edge [37,48]. This definition implies that

$$E_{\text{form}}(\text{vac}) = -2\omega_{\text{p}1} - 2\omega_{\text{p}2} - 2\omega_{\text{p}3} - 4\omega_{\text{p}4} - 2\omega_{\text{p}5} - 2\omega_{\text{p}6} - 4\omega_{\text{p}7} - 4\omega_{\text{p}8} - \dots \\ -8\omega_{\text{t}1} - 4\omega_{\text{t}2} - 16\omega_{\text{t}3} - 8\omega_{\text{t}4} - 16\omega_{\text{t}5} - 4\omega_{\text{t}6} - 8\omega_{\text{t}7} - \dots - 3\omega_{\text{q}1} - \dots \approx 0.279 \text{ eV}. \quad (16)$$

$E_{\text{form}}(\text{vac})$ differs from $E_{\text{form}}(\text{ad})$ due to the presence of many-body interactions.

(ii) *Ostwald ripening.* Using the formation energies obtained in Sec. V A, we can describe some consequences for Ostwald ripening [48]. The effective activation energy for Ostwald ripening of “adatom” islands is given by $E_{\text{OR}}(\text{ad}) \approx E_{\text{d}} + E_{\text{form}}(\text{ad}) = 0.388 + 0.349 = 0.737 \text{ eV}$, where we reasonably assume no additional barrier for attachment to ascending steps [48]. However, as noted in Sec. I, we expect Smoluchowski rather than Ostwald ripening to dominate adatom island coarsening. The effective barrier for Ostwald ripening of “vacancy” islands is $E_{\text{OR}}(\text{vac}) = E_{\text{d}}(\text{vac}) + E_{\text{form}}(\text{vac})$. In principle, the diffusion barrier for isolated vacancies, $E_{\text{d}}(\text{vac})$ can be determined from a sufficiently complete set of unconventional ϕ -interactions. However, we perform a more direct analysis using a 4×4 unit cell to obtain $E_{\text{d}}(\text{vac}) \approx 0.264 \text{ eV}$. This result implies that $E_{\text{OR}}(\text{vac}) \approx 0.264 + 0.279 = 0.543 \text{ eV}$.

(iii) *Island nucleation kinetics.* A conventional treatment, in which longer-range interactions are negligible, suggests that the island density, N_{isl} , for irreversible island formation at lower T is controlled by E_{d} via $N_{\text{isl}} \approx 0.47(F/\nu)^{1/3} e^{E_{\text{d}}/(3k_{\text{B}}T)}$ per adsorption site, where F is the deposition flux and ν is the prefactor for hopping [11]. If ad-dimer diffusion is not significant, then the above conventional treatment also indicates that the critical temperature T_{c} for the transition to reversible island formation satisfies $(\nu/F)e^{-(E_{\text{d}}+1.5|\omega_{\text{p}1}|)/(k_{\text{B}}T_{\text{c}})} \approx 10$ [11]. This implies that $T_{\text{c}} \approx 240 \text{ K}$ for Ag/Fe(100) when $F = 5 \times 10^{-3} \text{ ML/s}$ and $\nu = 5 \times 10^{12} \text{ /s}$. However, there are some caveats to the above analysis. *First*, it is expected that the repulsive component of the pair interactions will inhibit aggregation (as well as nucleation) leading to an enhancement of island density

relative to the above prediction [12,13,49]. *Second*, we can determine the barrier for ad-dimer diffusion as $E_{d2} = E_d - \omega_{p1} + \phi_{p1} \approx 0.41$ eV. This barrier is low enough that dimer diffusion should impact the island density. *Third*, one could argue that, for nucleation studies, interaction parameters from large-unit-cell calculations allowing full relaxation of isolated adatoms and adatom pairs are more appropriate than those from CE analysis. Using the corresponding ω_{p1} from Appendix D instead gives $T_c \approx 140$ K and $E_{d2} \approx 0.33$ eV.

(iv) *Periphery diffusion*. Using ω - and ϕ -interactions obtained in Secs. III and IV, we consider periphery diffusion focusing on diffusion along close-packed step edges. Using the total interaction energies in the initial state and the TS

$$\begin{aligned} \Phi_{\text{init}} = & \omega_{p1} + 2\omega_{p2} + \omega_{p3} + 4\omega_{p4} + 2\omega_{p5} + \omega_{p6} + 4\omega_{p7} + 4\omega_{p8} + \dots \\ & + 2\omega_{t1} + \omega_{t2} + 6\omega_{t3} + 3\omega_{t4} + 4\omega_{t5} + 2\omega_{t6} + 2\omega_{t7} + \dots \approx -0.225 \text{ eV}, \end{aligned} \quad (17)$$

and

$$\Phi_{\text{TS}} = 2\phi_{p1} + \phi_{t1} + 2\phi_{t2} + 2\phi_{t3} + \dots, \quad (18)$$

the values of ϕ_{p1} , ϕ_{t1} , and ϕ_{t2} in Sec. IV B, and anticipating a significant attractive trio interaction ϕ_{t3} comparable to ω_{p2} based studies of other metal (100) systems [18] suggests a rough estimate of $\Phi_{\text{TS}} \approx -0.22 + 2\phi_{t3} \approx -0.32$ eV. This result leads to an edge diffusion barrier of $E_e = E_d + \Phi_{\text{TS}} - \Phi_{\text{init}} \approx 0.29$ eV. We have also performed a more direct DFT calculation of E_e using a 4×4 unit cell with a double row of atoms representing the step edge and including a single edge adatom to obtain $E_e \approx 0.251$ eV.

VI. CONCLUSIONS

We assess the energetics relevant for submonolayer epitaxial films of Ag on Fe(100). Our most detailed analysis is for the conventional ω -interactions (between Ag adatoms at 4fh sites) which control adlayer thermodynamics. As expected based on analysis of other metal (100) systems, short-range pair interactions ω_{p1} and ω_{p2} , as well as compact trio interactions, ω_{t1} and ω_{t2} , dominate over longer-range pair and other trio interactions. However, utilizing an extensive CE analysis, we find unexpectedly robust oscillatory decay of longer-range pair ω -interactions with increasing separation, and show that these interactions must be included for a reliable analysis of adlayer energetics. This robust oscillatory decay also applies to trio ω -interactions with increasing perimeter length of the trio motif. For analysis of the kinetics of adlayer formation during deposition and of post-deposition coarsening, it is also necessary to assess surface diffusion barriers which for general local environments of the adatom. These barriers can be determined with the aid of a separate set of unconventional ϕ -interactions involving one adatom at the bridge site which is the TS for hopping and the others at 4fh sites. We describe the additional challenges associated with a CE analysis of these ϕ -interactions, and present a targeted analysis of the two shortest-range pair ϕ -interactions and of the most compact trio ϕ -interaction which are expected to dominate other ϕ -interactions.

This extensive knowledge of lateral interactions, together with our analysis of the terrace diffusion barrier for isolated Ag adatoms, allows characterization of the nucleation and growth of two-dimensional Ag adatom islands on Fe(100), and of the post-deposition

coarsening and sintering of such islands and of vacancy pits. The key energetic parameters controlling these various phenomena are also presented.

ACKNOWLEDGEMENTS

WL and LH acknowledge support from startup funds from the South University of Science and Technology of China and from NSFC under Grant No. 11404160. JWE and YH were supported for this work by NSF grants CHE-1111500 and CHE-1507223, and their work was performed at Ames Laboratory which is operated for the US Department of Energy by Iowa State University under Contract No. DE-AC02-07CH11358. Computations utilized USDOE NERSC, OLCF, and NSF-supported XSEDE resources.

APPENDIX A: BENCHMARK DFT ANALYSES

Our DFT analysis for a bulk bcc Fe crystal chooses the primitive cell as the supercell with one Fe atom. The \mathbf{k} mesh is taken to be $51 \times 51 \times 51$, which is large enough for energy convergence. The energy cutoff is set to be the VASP default value 267.882 eV. A test increasing the energy cutoff to 400.000 eV causes a negligible energy change of only about 2 meV per Fe atom. Using the PAW PBE GGA functional as described in Sec. II, we find that the total energy E_T is lowest when the lattice constants $a = 0.2830$ nm (cf. the experimental value 0.2866 nm at room temperature [33]) and the magnetic moment per atom, $\mu = 2.1985\mu_B$ (cf. the experimental value $2.216\mu_B$ at 0 K [50]), where μ_B is the Bohr magneton. The cohesive energy $E_c = E_{Fe} - E_T = 4.860$ eV (cf. the experimental value 4.28 eV at 0 K [51]), where E_{Fe} is the energy of one Fe atom in gas phase.

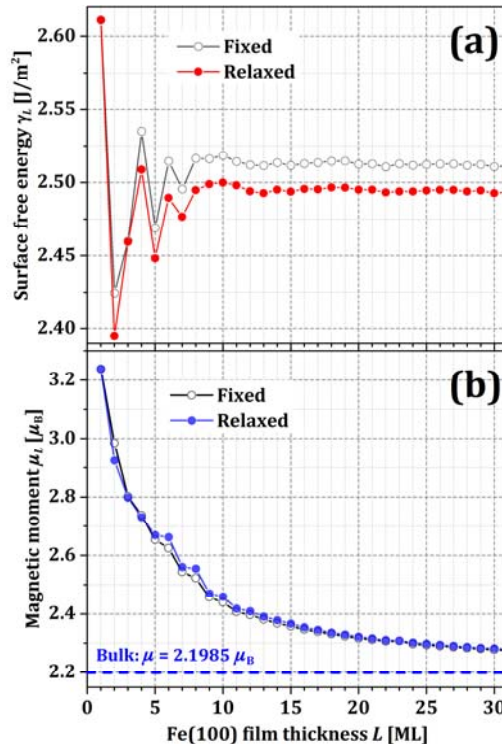


FIG. 6. (Color online) (a) Surface free energy γ_L and (b) magnetic moment, μ_L , per Fe atom from our DFT calculations versus thickness L for fixed and relaxed Fe(100) films.

Our surface-energy calculation for a Fe(100) slab with a thickness of L (in units of ML) uses a 1×1 lateral supercell. The vacuum thickness is not less than 1.5 nm, and the \mathbf{k} mesh is always $51 \times 51 \times 1$. The surface energy is calculated as [36,38,52]

$$\gamma_L = \frac{E_{\text{tot}} - N_L \sigma_{\text{bulk}}}{2A}, \quad (19)$$

where E_{tot} is the DFT total energy of the slab in the supercell, N_L is the total number of atoms in the slab with a thickness L , $\sigma_{\text{bulk}} = E_{\text{T}}$ is the DFT energy per Fe atom in bulk bcc Fe, and $A = a^2$ is the area of a free face of the 1×1 slab. Figure 6(a) shows the obtained surface energies γ_L for both “fixed” and “relaxed” slabs. The oscillations in γ_L versus L , as shown in Fig. 6(a), are generally attributed to QSE on metal films [35,36,38]. With increasing L , the value of γ_L approaches “bulk” surface energy. From Fig. 6(a), $\gamma_{L=31} = 2.493$ and 2.511 J/m² for the “relaxed” and “fixed” Fe(100) film, respectively. These values reasonably match the experimental estimate of 2.417 J/m² at the melting point of Fe [53], versus a previous DFT value 2.222 J/m² for Fe(100) film [54]. Figure 6(b) shows the magnetic moments μ_L calculated for both “fixed” and “relaxed” slabs. We find that μ_L versus L displays slightly oscillatory decay for $L < 13$, and then smooth decay for larger L toward the bulk value of $2.1985\mu_B$, see Fig. 6(b).

We also perform analysis for a bulk fcc Ag crystal. Using the \mathbf{k} mesh of $61 \times 61 \times 61$, and the VASP default energy cutoff of 249.844 eV for Ag, we obtain the lattice constant of 0.4152 nm (cf. the experimental value 0.4069 nm at 0 K [34]), corresponding to a surface lattice constant of $0.4152/\sqrt{2} = 0.2936$ nm, which has a mismatch of only 3.7% relative to the above DFT lattice constant 0.2830 nm for bcc Fe crystal. The cohesive energy is 2.520 eV (cf. the experimental value 2.95 eV at 0 K [51]).

APPENDIX B: REFINED CE ANALYSIS WITH SIXTEEN ω 's

Our extensive CE modeling in Sec. III B incorporating sixteen ω -interactions including 8 pairs and 7 trios, and 1 square quartet uses subsets of 17 configurations selected out of a larger set of 20 configurations to determine these ω 's and $E_{4\text{fh}}$. See Table II. The 20 configurations are shown in Fig. 7, and the corresponding DFT adlayer energies per Ag atom are listed in Table III. In addition, we assess the dependence of adlayer energy per Ag atom on Fe(100) slab thickness. Table III shows results for selected configurations for 8-, 10-, and 15-ML slabs. In these calculations for total energies of slabs, we always relax topmost 5 ML of an Fe(100) slab, and keep other underlying ML fixed.

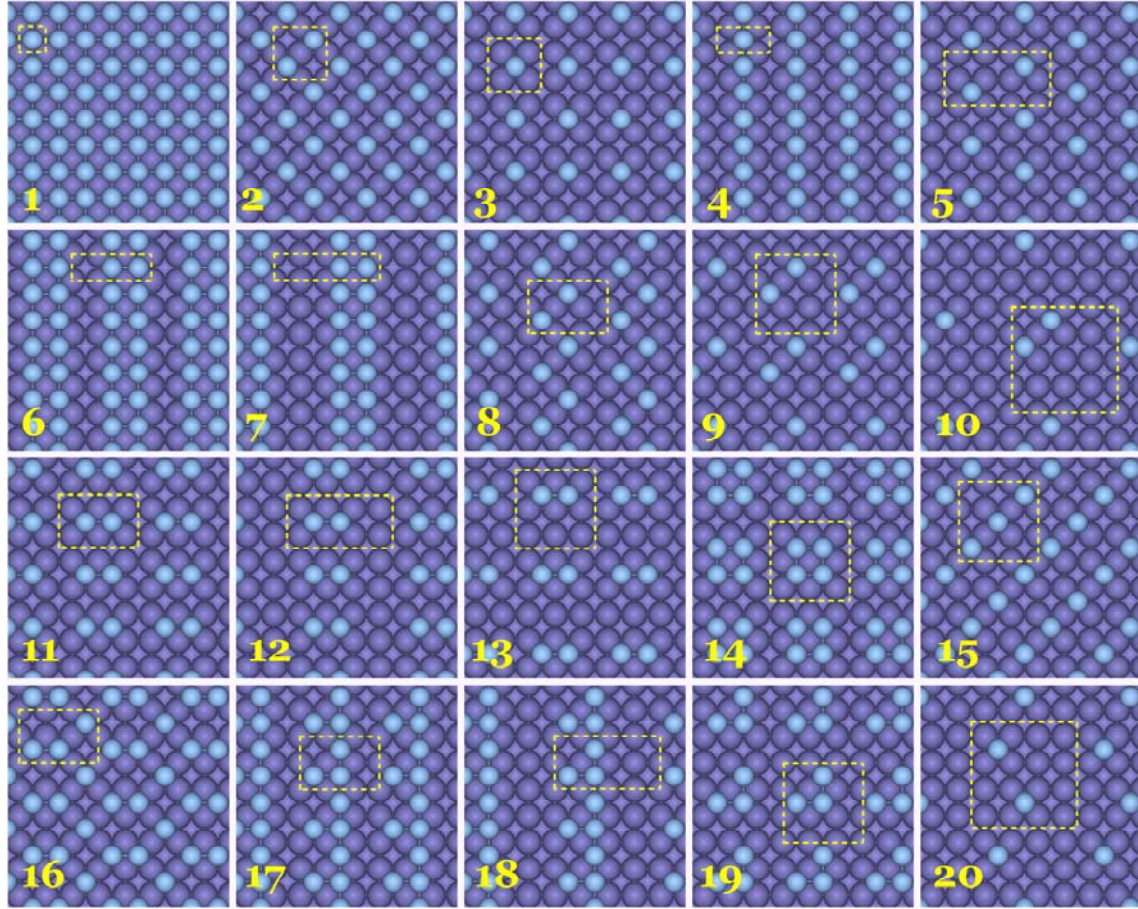


FIG. 7. (Color online) The 20 configurations, numbered from 1 to 20, used to determine ω -interactions and $E_{4\text{fh}}$. The corresponding adlayer energies per atom are listed in Table III.

Table II Eight choices (A–H) of the 3 configurations omitted out of 20 in the leave-3-out cross-validation method for determining $E_{4\text{th}}$ and sixteen ω 's. These configurations are shown in Fig. 7.

Choice	Three omitted configurations		
A	6	8	18
B	6	18	19
C	6	8	19
D	6	7	8
E	8	18	19
F	7	8	19
G	7	8	14
H	5	8	19

Table III Adlayer energies (in eV) per Ag atom for 20 configurations numbered as in Fig. 7 and described by notations in the second column. All these energies are obtained from Eq. (1). The third column is the \mathbf{k} mesh used in the DFT total-energy calculations for 8-, 10-, and 15-ML Fe(100) slabs.

No.	Notation	\mathbf{k} mesh	8-ML slab	10-ML slab	15-ML slab
1	$E_{1\times 1}^{1h}$	21×21	-2.855	-2.854	-2.853
2	$E_{c(2\times 2)}^{2h}$	11×11	-2.566	-2.566	-2.556
3	$E_{2\times 2}^{2h}$	11×11	-2.492	-2.497	-2.483
4	$E_{2\times 1}^{1h}$	11×21	-2.722	-2.702	-2.696
5	$E_{2\times 2,p4}^{2h}$	11×11			-2.476
6	$E_{3\times 1}^{2h}$	7×21	-2.756	-2.756	-2.754
7	$E_{4\times 1,p1}^{2h}$	5×21			-2.750
8	$E_{3\times 2,p2}^{2h}$	7×11			-2.522
9	$E_{3\times 3,p2}^{2h}$	7×7			-2.511
10	$E_{4\times 4,p2}^{2h}$	5×5			-2.539
11	$E_{3\times 2,p1}^{2h}$	7×11			-2.571
12	$E_{4\times 2,p1}^{2h}$	5×11			-2.585
13	$E_{3\times 3,p1}^{2h}$	7×7			-2.579
14	$E_{3\times 3,q1}^{4h}$	7×7			-2.640
15	$E_{3\times 3,t6}^{3h}$	7×7			-2.528
16	$E_{3\times 2,t3}^{3h}$	7×11			-2.597
17	$E_{3\times 2,t1}^{3h}$	7×11			-2.684
18	$E_{4\times 2,t1}^{3h}$	5×11			-2.679
19	$E_{3\times 3,t1}^{3h}$	7×7			-2.602
20	$E_{4\times 4,p4}^{2h}$	5×5			-2.498
	$E_{4\times 4}^{1h}$	5×5	-2.549	-2.541	-2.529
	$E_{4\times 4}^{1b}$	5×5	-2.160	-2.155	-2.141

APPENDIX C: ADDITIONAL COMMENTS ON CLUSTER EXPANSION ANALYSIS

In Sec. III, we noted that selecting configurations only with smaller unit cells to determine $E_{4\text{fh}}$ and ω 's may yield an effective value of $\tilde{E}_{4\text{fh}}$ (due to incorporation of neglected longer-range interactions) and more accurate estimates of ω 's (due to cancellation of the effects of such interactions). For a simple example of this effect, consider a system which is described exactly by three pair interactions, ω_{p1} , ω_{p2} , and ω_{p3} , plus a bent trio interaction ω_{t1} , in addition to an adsorption energy, $E_{4\text{fh}}$. Suppose, however, that we try to describe the system with only three interactions $\tilde{\omega}_{p1}$, $\tilde{\omega}_{p2}$, and $\tilde{\omega}_{t1}$ effectively ignoring the presence of the "longer-range" interaction ω_{p3} . Consider determination of these three $\tilde{\omega}$'s as well as the effective adsorption energy $\tilde{E}_{4\text{fh}}$ from the energies $E_{1\times 1}^{1h}$, $E_{c(2\times 2)}^{2h}$, $E_{2\times 1}^{1h}$, and $E_{2\times 2}^{1h}$ for $p(1\times 1)$, $c(2\times 2)$, $p(2\times 1)$, and $p(2\times 2)$ configurations, respectively. Solution of the corresponding linear relations reveals that

$$\begin{cases} \tilde{E}_{4\text{fh}} = E_{4\text{fh}} + 2\omega_{p3}, \\ \tilde{\omega}_{p1} = \omega_{p1}, \\ \tilde{\omega}_{p2} = \omega_{p2}, \\ \tilde{\omega}_{t1} = \omega_{t1}, \end{cases} \quad (20)$$

i.e., the effective $\tilde{E}_{4\text{fh}}$ incorporates the fully neglected pair interaction ω_{p3} and thus the $\tilde{\omega}$'s recover exactly the corresponding true ω 's.

The same exact recovery is achieved in an extended model also including the linear trio ω_{t2} . In this case, one determines the four $\tilde{\omega}$'s as well as $\tilde{E}_{4\text{fh}}$ from the energies $E_{1\times 1}^{1h}$, $E_{c(2\times 2)}^{2h}$, $E_{2\times 1}^{1h}$, $E_{2\times 2}^{1h}$, and $E_{2\times 2}^{3h}$ for $p(1\times 1)$, $c(2\times 2)$, $p(2\times 1)$, $p(2\times 2)$, and $p(2\times 2)$ configurations, respectively. Solution of the corresponding linear relations is that

$$\begin{cases} \tilde{E}_{4\text{fh}} = E_{4\text{fh}} + 2\omega_{p3}, \\ \tilde{\omega}_{p1} = \omega_{p1}, \\ \tilde{\omega}_{p2} = \omega_{p2}, \\ \tilde{\omega}_{t1} = \omega_{t1}, \\ \tilde{\omega}_{t2} = \omega_{t2}. \end{cases} \quad (21)$$

However, for more general models, $\tilde{E}_{4\text{fh}}$ will only partly incorporate the effect of neglected long range ω 's and the $\tilde{\omega}$ will not exactly equal the corresponding true ω .

In Sec. III A, we presented a preliminary analysis of conventional interactions just retaining ω_{p1} , ω_{p2} , ω_{t1} , and ω_{t2} as the expected dominant interactions, and determining $E_{4\text{fh}}$ separately and directly either from the energy of a $p(2\times 2)$ or $p(4\times 4)$ configuration. Here, the four ω 's were determined from the equations

$$\begin{cases} E_{1\times 1}^{1h} = E_{4\text{fh}} + 2\omega_{p1} + 2\omega_{p2} + 4\omega_{t1} + 2\omega_{t2}, \\ E_{c(2\times 2)}^{2h} = E_{4\text{fh}} + 2\omega_{p2}, \\ E_{2\times 1}^{1h} = E_{4\text{fh}} + \omega_{p1} + \omega_{t2}, \\ E_{3\times 1}^{2h} = E_{4\text{fh}} + \frac{3}{2}\omega_{p1} + \omega_{p2} + 2\omega_{t1} + \omega_{t2}, \end{cases} \quad (22)$$

for the energies per adatom in $p(1 \times 1)$, $c(2 \times 2)$, $p(2 \times 1)$, and $p(3 \times 1)$ configurations.

APPENDIX D: ELECTRONIC AND ELASTIC COMPONENTS OF INTERACTIONS

As indicated in Sec. III. C, it is instructive to compare results for lateral interactions using a relaxed substrate to obtain the total interaction and a frozen substrate to obtain the corresponding electronic component of the interaction. The difference between the total interaction and its electronic component gives the elastic component. We have performed such a comparative analysis for first and second NN pairs, as well as one bent trio configuration, using a 5×5 unit cell which is larger than those used in the above CE analysis, for 4-, 8-, and 12-ML Fe(100) slabs. From this sequence of calculations, limiting behavior for a semi-infinite slab is evident, see Table IV. As noted in Sec. III C, the elastic component of the interactions remains significant in this limit. We comment here further on the feature that these results for just the electronic component of the interactions are closer to the results of our CE analysis in Table I. These CE results were obtained with a relaxed substrate, and thus by default might be regarded as corresponding to total interactions. However, a general feature of CE analyses is that energies are obtained from adlayer configurations with small-unit-cell periodicities including a $p(1 \times 1)$ configuration. Such small unit cells limit lateral relaxation of substrate atoms near the adsorbed atoms, relative to the more substantial relaxation which can occur for isolated adatoms or small clusters of adatoms in large-unit-cell analysis. The optimal selection of (generally effective) interactions of adlayer atoms depends on the application of interest. For nucleation studies focused on diffusion of isolated adatoms and formation of small clusters, the values from larger-unit-cell calculations are more appropriate. For analysis of phenomena involving higher-coverage configurations, such as cluster diffusion and sintering, results from CE analysis or refinements thereof are more appropriate.

Table IV Decomposition into the electronic and elastic components of the adsorption energy and ω -interactions (in eV) for Ag on 4-, 8-, and 12-ML Fe(100) slabs. E_{4fh} , ω_{p1} , ω_{p2} , and ω_{t1} are obtained from DFT total energies of configurations with one adatom, one first NN pair, one second NN pair, and one bent trio, respectively, on the slab using a 5×5 unit cell. The \mathbf{k} mesh for the 5×5 -unit-cell calculations is taken to be 5×5 . In the 8- and 12-ML slab calculations, we relax topmost 5 ML of Fe(100) slab, and keep the underlying layers fixed. For the 4-ML slab calculations, we relax topmost 3 ML and keep the bottom layer fixed.

Slab thickness		Electronic	Elastic	Total
4 ML	E_{4fh}	-2.511	-0.094	-2.606
	ω_{p1}	-0.166	+0.077	-0.088
	ω_{p2}	-0.049	+0.049	-0.000
	ω_{t1}	+0.050	-0.050	-0.000
8 ML	E_{4fh}	-2.485	-0.074	-2.559
	ω_{p1}	-0.171	+0.057	-0.114
	ω_{p2}	-0.043	+0.036	-0.008
	ω_{t1}	+0.045	-0.018	+0.027

12 ML	$E_{4\text{fh}}$	-2.482	-0.080	-2.562
	ω_{p1}	-0.175	+0.062	-0.113
	ω_{p2}	-0.042	+0.038	-0.004
	ω_{t1}	+0.047	-0.020	+0.027

REFERENCES

- [1] C. M. Wei and M. Y. Chou, Phys. Rev. B **68**, 125406 (2003).
- [2] J. J. Paggel, C. M. Wei, M. Y. Chou, D.-A. Luh, T. Miller, and T.-C. Chiang, Phys. Rev. B **66**, 233403 (2002).
- [3] J. J. Paggel, T. Miller, and T.-C. Chiang, Phys. Rev. Lett. **81**, 5632 (1998).
- [4] J. J. Paggel, T. Miller, and T.-C. Chiang, Science **283**, 1709 (1999).
- [5] T. C. Chiang, Surf. Sci. Rep. **39**, 181 (2000).
- [6] J. J. Paggel, D.-A. Luh, T. Miller, and T.-C. Chiang, Phys. Rev. Lett. **92**, 186803 (2004).
- [7] T. Uchihashi and T. Nakayama, Surf. Sci. **637-638**, 58 (2015).
- [8] D.-A. Luh, T. Miller, J. J. Paggel, M. Y. Chou, and T.-C. Chiang, Science **292**, 1131 (2001).
- [9] K. L. Man, Z. Q. Qiu, and M. S. Altman, Phys. Rev. Lett. **93**, 236104 (2004).
- [10] K. L. Man, Z. Q. Qiu, and M. S. Altman, Phys. Rev. B **81**, 045426 (2010).
- [11] J. W. Evans, P. A. Thiel, and M. C. Bartelt, Surf. Sci. Rep. **61**, 1 (2006).
- [12] K. A. Fichthorn and M. Scheffler, Phys. Rev. Lett. **84**, 5371 (2000).
- [13] A. Bogicevic, S. Ovesson, P. Hyldgaard, B. I. Lundqvist, H. Brune, and D. R. Jennison, Phys. Rev. Lett. **85**, 1910 (2000).
- [14] J.-M. Wen, J. W. Evans, M. C. Bartelt, J. W. Burnett, and P. A. Thiel, Phys. Rev. Lett. **76**, 652 (1996).
- [15] P. A. Thiel, M. Shen, D.-J. Liu and J. W. Evans, J. Phys. Chem. C, **113**, 5047 (2009).
- [16] T. J. Stasevich, T. L. Einstein, and S. Stolbov, Phys. Rev. B **73**, 115426 (2006).
- [17] T. L. Einstein and R. Sathiyarayanan, in *Nanophenomena at Surfaces*, Springer Series in Surface Sciences 47, M. Michailov, ed. (Springer, Berlin, 2011), Ch. 2.
- [18] Y. Han, D.-J. Liu, and J. W. Evans, Nano Lett. **14**, 4646 (2014).
- [19] Y. Han and J. W. Evans, J. Phys. Chem. Lett. **6**, 2194 (2015).
- [20] Y. Han, B. Ünal, D. Jing, P. A. Thiel, and J. W. Evans, J. Chem. Phys. **135**, 084706 (2011).
- [21] Y. Han, B. Ünal, and J. W. Evans, Phys. Rev. Lett. **108**, 216102 (2012).
- [22] C. Stampfl, Catal. Today **105**, 17 (2005).
- [23] L. M. Herder, J. M. Bray and W. F. Schneider, Surf. Sci. **640**, 104 (2015).
- [24] W. Luo and K. A. Fichthorn, Phys. Rev. B **72**, 115433 (2005).

- [25] J. D. Howe, P. Bhopale, Y. Tiwary, and K. A. Fichthorn, *Phys. Rev. B* **81**, 121410 (2010).
- [26] G. Kresse and J. Hafner, *Phys. Rev. B* **47**, 558 (1993).
- [27] G. Kresse and J. Hafner, *Phys. Rev. B* **49**, 14251 (1994).
- [28] G. Kresse and J. Furthmüller, *J. Comput. Mat. Sci.* **6**, 15 (1996).
- [29] G. Kresse and J. Furthmüller, *Phys. Rev. B* **54**, 11169 (1996).
- [30] P. E. Blochl, *Phys. Rev. B* **50**, 17953 (1994).
- [31] G. Kresse and D. Joubert, *Phys. Rev. B* **59**, 1758 (1999).
- [32] J. P. Perdew, K. Burke, and M. Ernzerhof, *Phys. Rev. Lett.* **77**, 3865 (1996).
- [33] E. R. Jette and F. Foote, *J. Chem. Phys.* **3**, 605 (1935).
- [34] A. K. Giri and G. B. Mitra, *J. Phys. D* **18**, L75 (1985).
- [35] F. K. Schulte, *Surf. Sci.* **55**, 427 (1976).
- [36] Y. Han and D.-J. Liu, *Phys. Rev. B* **80**, 155404 (2009).
- [37] D.-J. Liu, *Phys. Rev. B* **81**, 035415 (2010).
- [38] Y. Han, B. Ünal, D. Jing, P. A. Thiel, J. W. Evans, and D.-J. Liu, *Materials* **3**, 3965 (2010).
- [39] J. Shao, *J. Am. Stat. Assoc.* **88**, 486 (1993).
- [40] P. Hyldgaard and T. L. Einstein, *Europhys. Lett.* **59**, 265 (2002).
- [41] Y. Tiwary and K. A. Fichthorn, *Phys. Rev. B* **75**, 235451 (2007).
- [42] Y. Tiwary and K. A. Fichthorn, *Phys. Rev. B* **78**, 205418 (2008).
- [43] G. Henkelman and H. Jónsson, *J. Chem. Phys.* **113**, 9978 (2000).
- [44] V. P. Zhdanov, *Elementary Physicochemical Processes on Solid Surfaces* (Plenum, New York, 1991).
- [45] H. Mehl, O. Biham, I. Furman, and M. Karimi, *Phys. Rev. B* **60**, 2106 (1999).
- [46] Y. Tiwary and K.A. Fichthorn, *Phys. Rev. B* **81**, 195421 (2010).
- [47] D.-J. Liu and J. W. Evans, *ChemPhysChem* **11**, 2174 (2010).
- [48] P. A. Thiel, M. Shen, D.-J. Liu and J.W. Evans, *J. Phys. Chem. C* **113**, 5047 (2009).
- [49] D. Kandel, *Phys. Rev. Lett.* **78**, 499 (1997).
- [50] H. Danan, A. Herr, and A. J. P. Meyer, *J. Appl. Phys.* **39**, 669 (1968).
- [51] C. Kittel, *Introduction to Solid State Physics*, 7th ed. (New York, John Wiley & Sons, Inc., 1996).
- [52] Y. Han, J. W. Evans, and D.-J. Liu, *Surf. Sci.* **602**, 2532 (2008).
- [53] W. R. Tyson and W. A. Miller, *Surf. Sci.* **62**, 267 (1977).
- [54] L. Vitos, A. V. Ruban, H. L. Skriver, J. Kollár, *Surf. Sci.* **411**, 186 (1998).